Microstructure and corrosion resistance of friction stir welded high nitrogen stainless steel joint

H. Zhang, D. Wang,‡,* P. Xue,‡,* L.H. Wu,* D.R. Ni,* B.L. Xiao,* and Z.Y. Ma**

** Shenyang National Laboratory for Materials Science, Institute of Metal Research, Chinese Academy of Sciences*

ARTICLE INFO

Article history:

Received Day Month Year,
Accepted Day Month Year
Available Day Month Year

Keywords:

Stainless steels
Intergranular corrosion
Pitting
Weld
Potentiodynamic
Potentiostatic

*Institute of Metal Research, Chinese Academy of Sciences, 72 Wenhua Road, Shenyang 110016, China.

‡ Corresponding authors: Tel./fax: +86-24-23971749 (D. Wang), Tel./fax: +86-24-23971752 (P. Xue); E-mail addresses: dongwang@imr.ac.cn (D. Wang), pxue@imr.ac.cn (P. Xue).

ABSTRACT

The corrosion resistance of a friction stir welded high nitrogen stainless steel joint was evaluated by immersion corrosion tests. The heavily corroded thermomechanically affected zone (TMAZ) was determined to be the weakest zone of the joint. The TMAZ, as a distinct transitional region with partial recrystallization, exhibited a non-uniform microstructure consisting of coarse and fine grains and an inhomogeneous strain distribution with high strain in fine grain regions. A higher corrosion rate was confirmed via electrochemical analyses, which was mainly attributed to the high defect density, galvanic corrosion and the formation of Cr-rich particles.

INTRODUCTION

High nitrogen stainless steel (HNS), as a promising engineering material, has gained more and more attention due to its favorable mechanical and corrosion properties. Nitrogen, as a powerful austenite-stabilizing element, can not only improve the strength and fracture toughness of HNS significantly, but also increase the pitting corrosion resistance of steel [1].

The corrosion resistance of HNS could be affected by many factors. Fu et al. [2] investigated the effects of cold working and sensitization treatment on the corrosion resistance of HNS, and the results showed that the high defect density introduced by cold working led to a less protective passive film. Similarly, it was found that pits were formed along deformation bands [3]. These results indicated that the corrosion resistance of HNS was affected by defect density, and highly related to the properties of passive film [4]. Alternatively, Lee et al. [5] analyzed the precipitates in HNS during aging, and a sigma phase, $M_{23}C_6$, M_6C, a chi phase, Cr_2N and AlN could be detected in the aged HNS. These precipitates exerted significant effects, not only on the mechanical properties and formability, but also on corrosion resistance [6-8].

Due to the high nitrogen content, the welding of HNS is a serious challenge [9], especially the welding of HNS thin sheets. Friction stir welding (FSW), as a solid-state joining method, is used to join low melting point materials due to its high joint efficiency, environmental friendliness and low residual stress and distortion [10-13]. With the development of welding tools, recent efforts have been dedicated to the welding of high melting point metals, such as stainless steels [14-16].

The properties of FSW stainless steel joints are very sensitive to heat input. It has been reported that the formation of sigma and intermetallic phases was observed in FSW austenitic stainless steel, leading to decreased corrosion resistance [17, 18]. However, in the case of a lean duplex stainless steel and ferritic stainless steel, no decrease of corrosion resistance was observed in the FSW joints [19, 20]. Therefore, to obtain FSW stainless steel joints with excellent corrosion resistance, the heat input, i.e., the welding parameters should be carefully controlled in order to prevent the formation of harmful phases. Furthermore, the FSW heat input should also be reduced for HNS to prevent the loss of nitrogen during welding [21-23].

During FSW, significant microstructural changes occur, forming four zones: the nugget zone (NZ) with fine equiaxed grains, the heat affected zone (HAZ) with a similar microstructure to that of the base metal (BM), and the thermomechanically affected zone (TMAZ) with a deformed structure. Due to their outstanding corrosion resistance, stainless steels are often applied in harsh service environments. Thus, identifying the most susceptible zone to corrosion in welded joints is a very important part of evaluating the safety of the welded structure [24-26].

It should be noted that the TMAZ, as a narrow transition zone affected by both mechanical deformation and thermal cycling, might exhibit a special corrosion behavior. The high defect density and possible precipitation could make the TMAZ the weakest zone of the FSW joints, whereas the fusion line and HAZs are more vulnerable to corrosion in the joints of fusion welding [27-30]. Unfortunately, the microstructural evolution and corrosion behavior of the TMAZ in the FSW HNS joint has received little attention, though defect-free joints of HNS have been achieved via FSW [15, 22, 31].

In this study, the microstructural evolution and corrosion behavior of the TMAZ in a FSW joint of HNS were studied in detail. It was proven that the TMAZ was indeed more sensitive to corrosion compared to other zones and therefore was the weakest zone of the whole joint. The mechanism responsible for this weakening was analyzed and discussed in detail.

Material and methods

Materials and welding parameters

Lab HNS sheets with a thickness of 1.8 mm and a chemical composition of Fe-18.4Cr-15.8Mn-2.2Mo-0.66N-0.04C, solution treated at 1100 °C for 2 h, were used as the BM. In this study, low heat input welding

parameters were selected, in order to prevent the precipitation of harmful phases, however, if the heat input was too low, damage of the welding tool could occur. Therefore, FSW was performed at a rotation speed of 600 rpm and a transverse speed of 100 mm/min (the parameter will be abbreviated to 600-100 for simplicity). A W-Re alloy welding tool with an 11-mm-dia shoulder and a 1.6-mm-length cylindrical pin was selected for FSW (Fig. 1(a)). In order to avoid oxidation, an argon gas shield was used during the welding process.

Immersion corrosion tests

The cross-section of the joint was cut perpendicular to the welding direction for optical microscopy (OM) and scanning electron microscopy (SEM) observations, and the specimens were electrolytically etched in a 10% oxalic acid solution. Ferric chloride was used to evaluate the pitting corrosion resistance of the joint. Following Method A in the ASTM G48 standard, specimens were immersed in 6% $FeCl_3$ solution (by mass), with a temperature of 50 ± 2 °C, for 48 h. After the immersion test, the specimens were subjected to electrolytic etching to identify the different regions of the joint.

Intergranular corrosion resistance was tested using a ferric sulfate-sulfuric acid test in the ASTM A262-10 standard, the specimens were immersed in a boiling test solution for 24 and 60 h, respectively, in order to observe the evolution of corroded morphology of the TMAZ, and 3D surface microscopy (Keyence VHX-1000) was applied to examine the depth of corrosion.

Electrochemical tests

Due to the small area and complex microstructure of the TMAZ, the electrochemical test specimens were carefully prepared. The sampling method of the TMAZ specimens is illustrated in Fig. 1(b). Thin sheets parallel to the surface of the FSW joint were cut. After polishing and etching, the TMAZ was marked, as shown in Fig. 1(c) (~800 μm in width), then the other area of the specimens was sealed with the exposed area being 2.4 mm^2. Electrochemical studies were carried out in a three-electrode cell using a Gamry Interface 1000 potentiostat/galvanostat at room temperature. A saturated calomel electrode (SCE) was selected as the reference electrode, a platinum plate served as the counter electrode and thin sheets cut from different zones of the FSW joint as the working electrode. All electrochemical experiments were carried out in a 3.5 wt.% NaCl solution.

Potentiodynamic polarization measurements were performed at a scan rate of 0.5 mV/s from -0.5 V with respect to the open-circuit potential to 1 V. The potentiostatic polarization test was conducted at 0.35 V_{SCE} based on the passive range obtained from potentiodynamic polarization tests.

Microstructural observation

The electron backscattered diffraction (EBSD) specimens were prepared by electropolishing with a 10% perchloric acid and 90% ethanol solution at -30 °C. Strain distribution map was calculated based on the misorientation within grains, the detailed description could be found in ref. [32]. The transmission electron microscopy (TEM, FEI Tecnai G2 F20) specimens were prepared through twin-jet electropolishing with the same solution as for EBSD specimens.

Results and discussion

Macrostructure of FSW HNS joint

The typical cross-sectional macrograph of the FSW joint is shown in Fig. 2(a). A sound joint with no macro defects was obtained. In our previous work [33], the microstructural evolution of the NZ was studied. In the TMAZ (Fig. 2(b)), the grains were very inhomogeneous and exhibited a highly deformed microstructure. Coarse elongated grains were distributed along the boundary between the NZ and TMAZ, with fine grains filling between the coarse ones. Clearly, the microstructure of the TMAZ exhibited transitional characteristics between the HAZ and NZ.

Identification of the weakest zone of the FSW joint by immersion corrosion tests

The morphology of the corroded surface after the pitting immersion corrosion test is shown in Fig. 3. While the number of pits in the NZ decreased significantly, the distribution and size of the pits in the HAZ were similar to those in the BM. In the TMAZ, however, pits distributed along the boundary of the NZ could be clearly observed. Since the area of the TMAZ was relatively small, the distribution density of pits in the TMAZ was very high. It is worth stressing that a high density of pits was observed in the TMAZs of various FSW HNS joints with common welding parameters for HNS, such as 500-50 and 400-100 (Fig. 3(a) and (b)). The distribution of pits was very similar in these joints, therefore in this study, only the 600-100 joint (Fig. 3(c)) was subjected to detailed analyses. From the magnified microstructure (Fig. 3(d)) many small pits could be observed around the fine grains in the TMAZ.

The pits in the homogeneous microstructure (the NZ and BM) were randomly distributed, however, in the TMAZ, the distribution of pits was highly related to the microstructure. The detailed pitting corrosion morphology of the TMAZ of the 600-100 joint is shown in Fig. 4(a). As can be clearly observed, small pits were found around fine grains, while few pits were observed around coarser ones, i.e., the fine grain region showed a higher tendency of pitting. Fig. 4(b) shows the corroded surface after immersion in a ferric sulfate-sulfuric acid solution for 24 h. The grain boundaries of coarse grains presented a ditch-like microstructure, while the fine grains were heavily corroded. However, the corroded morphology of fine grains in the TMAZ was different from that in the NZ, though the grain size was approximately the same. The fine grains in the NZ were evenly corroded and the corroded pits were relatively shallow, whereas the fine grains in the TMAZ evolved into deep pits. Clearly, the TMAZ showed different corrosion behavior.

After the long-term intergranular corrosion test for 60 h, the TMAZ was heavily corroded and developed into deep ditches, as shown in Fig. 5(a). Fig. 5(b) shows a 3D surface corrosion morphology around the TMAZ. The TMAZ exhibited the largest corrosion depth of ~100 μm. From the results of immersion tests, it was obvious that the TMAZ was more susceptible to corrosion. The microstructural difference between TMAZ, NZ and HAZ, or even between the fine grains and coarse grains within the TMAZ, could cause galvanic corrosion [34, 35], and the corrosion rate would be accelerated, leading to the ditch-like structure shown in Fig. 5(a). The heavily corroded TMAZ observed in Figs. 4(b) and 5 could have harmful effects on the mechanical properties of the joint due to the deep pits and thickness reduction. The welded structure when exposed in aggressive medium may fail at this special transitional zone.

Electrochemical tests for different zones of FSW joint

Potentiodynamic polarization diagrams are given in Fig. 6. A range of passivity beyond the open-circuit potential could be well observed in each curve. It should be noted that the curves of the BM and the NZ showed little difference, while the passive range of the TMAZ became significantly narrower. The values of the corrosion potentials E_{corr},

transpassive potentials E_{tr} and passive current densities I_p were calculated from the curves and are presented in Table 1. It is clear that the TMAZ showed significantly higher I_p than the BM and NZ. The E_{tr} of the TMAZ also decreased sharply compared to that of the BM and NZ. Thus, a higher corrosion rate and larger tendency for film dissolution were confirmed in the TMAZ.

Fig. 7 shows the current-time transients of HNS in 3.5 wt.% NaCl. Each current transient represents the initiation, temporary propagation and repassivation of an unstable micropit [36, 37]. The current densities decreased rapidly in the first stage, indicating the nucleation and growth of the passive film. A further increase in time led to a more stable current density, which was the result of the balance of passive film growth and dissolution. The curve of the TMAZ showed major differences compared to that of the BM and the NZ. It took much more time for the TMAZ to achieve a steady current density, and numerous current transients could be clearly observed. All these evidences indicated that a less protective passive film was formed in the TMAZ.

The TMAZ, as a transition zone affected by both welding thermal cycle and deformation, might respond differently to corrosion media. The current response with time can be described by the following formula [38]:

$$i(t) = 10^{-(U+k \lg t)} \quad (1)$$

where *i(t)* represents the current density, *U* is a constant, *t* is time and *k* is the slope of the double-log plot for potentiostatic polarization.

k is usually considered to be related to the compactness of the passive film [39-41], *k* = -1 indicates the formation of a compact, highly protective passive film, while *k* = -0.5 represents that the passive film is porous and less protective. Fig. 8 shows the double-log plots of current density vs. time of different zones of the FSW joint. The slopes of the BM and the NZ were -0.913±0.011 and -0.833±0.004, respectively, while the slope of the TMAZ was -0.762±0.012. Clearly, the passive film in the TMAZ was less compact, therefore, the corrosion resistance was decreased. During immersion, the rate of local dissolution and repassivation of the passive film mainly determined the corrosion resistance of the material. Therefore, the long-term corrosion behavior was highly related to the repassivation behavior. The *cBV* value, as an important parameter of repassivation rate, could be calculated via the following formula [42, 43]:

$$\log i(t) = \log A + \frac{cBV}{Q(t)} \quad (2)$$

where *A* and *B* are constant parameters, V is the potential drop across the film, *Q*(*t*) is the charged density which is the integration of the current density with time, and *c* is *zFρ*/2.3*M.* For *zFρ*/2.3*M*, z is the number of electrons transferred for a metal ion, F is the Faraday constant, q is the density of oxide films, and M is the molecular mass of oxide film.

Fig. 9 shows the log*i*(*t*) versus 1/*Q*(*t*) plot, the *cBV* value of the TMAZ was 0.0158±0.0012, which was significantly larger than those of the NZ and BM (0.0072 ± 0.0003 and 0.0107 ± 0.0001, respectively). Therefore, the repassivation rate of the TMAZ was significantly lower, leading to inferior corrosion resistance in long-term corrosion resistance tests.

Microstructural characterization of TMAZ

In order to investigate the reasons for the inferior corrosion resistance in the TMAZ, detailed microstructure examinations of the TMAZ were conducted. EBSD maps of the TMAZ are presented in Fig. 10. A typical deformed microstructure could be observed in Fig. 10(a), and a high density of low angle grain boundaries (LAGBs, <15°, white line) distributed in this transitional region indicates that severe deformation occurred around the welding tool during FSW. It should be noted that in the coarse grain regions, the LAGB distribution was inhomogeneous within the grains. The LAGBs developed mainly in the neighborhoods of the original grain boundaries, and arranged as roughly parallel bands along the longitudinal direction of these coarse grains. In the regions with small-sized grains, however, the distribution of LAGBs was relatively homogeneous, and sub-grain boundaries could be well observed within these grains (Fig. 10(b)).

There are several interesting phenomena that could help with understanding the dynamic recrystallization process in the TMAZ. As shown in Fig. 10(b), some discontinuous high angle grain boundaries (HAGBs, ≥15°, black line) were formed inside the grains; it could be explained by accumulated misorientation, which was the mechanism of continuous dynamic recrystallization (CDRX). On the other hand, local bulge phenomenon also existed in some grains, and this indicates that discontinuous dynamic recrystallization (DDRX) also occurred during FSW in the TMAZ.

During the welding process, the temperature in the NZ was relatively high, thus complete recrystallization took place, leading to an equiaxed grain microstructure (Fig. 10(c)). The TMAZ, on the other hand, exhibited a partially recrystallized microstructure due to the lower temperature and insufficient deformation. The necklace-like microstructure with fine grains and coarse grains in the TMAZ could be attributed to the CDRX and DDRX, and the newly formed fine grains also contained some substructures, which might be associated with the high cooling rate of FSW.

The strain contouring map of the TMAZ shows that high strain was concentrated in fine grain regions (Fig. 10(d)). It should be emphasized that the corrosion morphologies obtained in Figs. 4(a) and (b) show that, the fine grain regions, i.e., the strain concentration regions, had a greater tendency of pitting. These high stress regions could be potential pitting sites due to their low barrier energy. Meanwhile, the high defect density could lead to an increase in free energy. All of these factors exerted a detrimental effect on the stability of the passive film [44], thereby reducing the corrosion resistance of the TMAZ, which is consistent with previous works [2, 3]. Zhang et al. [45] also found that with increasing applied stress, the corrosion resistance decreased significantly.

Fig. 11(a) shows the typical morphology of fine grains in the TMAZ. Sub-grains could be clearly observed. It can be deduced that dynamic recovery occurred in the initial stages of the welding process. The dislocations were gradually absorbed by the sub-grain boundaries and developed into a network or wall structure. As a result, the dislocation density within grains was significantly decreased, and the misorientation of the LAGBs increased with the absorption of dislocations, resulting in the transformation from LAGBs to HAGBs, as observed in Fig. 10(b). Alternatively, due to the severe deformation, the defect density increased significantly and deformation twins were formed (Fig. 11(b)) within some grains in the TMAZ, and these high defect density regions could become potential sites for corrosion.

At some grain boundaries of the TMAZ, a newly formed secondary phase was observed. As shown in Fig. 11(c), precipitated particle with a size of ~200 nm was found in grain boundary junctions. Via the selected area diffraction pattern, the precipitation was identified as the χ (chi) phase, which had a BCC structure and a chemical formula of $Cr_{12}Fe_{36}Mo_{10}$. The formation of this Cr- and Mo-containing phase

would lead to a decrease in the corrosion resistance due to the appearance of a Cr- and Mo-depleted zone, as observed in Fig. 11(d), and the reduction of Cr and Mo could also result in a less protective passive film.

The χ phase is considered a metastable phase precipitated before the σ (sigma) phase, and the σ phase could seriously deteriorate the corrosion resistance of stainless steel. In our study, no σ phase was detected in the TMAZ or the NZ, attributed to the high cooling rate of FSW. It has been reported that the precipitation of Cr_2N could be detected in the HNS during thermal cycling [8, 21, 46] and Cr_2N have harmful effects on the corrosion resistance. However, in this study, no Cr_2N phase was observed, which should also be attributed to the high cooling rate during the welding of 2 mm thick sheets.

It was previously reported that it usually took hours for χ phase to precipitate [5]. In this study, however, the formation of χ phase was significantly accelerated in the TMAZ, attributed to the following two factors. First, intense plastic deformation accelerated the diffusion of elements [47], thereby accelerating the precipitation of the χ phase particles. Second, the size of the χ phase particles was very fine, resulting in less time taken for precipitation. The fine and small amount of χ phase had harmful effects on the corrosion resistance of the TMAZ, but the high defect density was the main reason of the TMAZ being the weakest zone to corrosion.

The corrosion behavior of the TMAZ is illustrated in Fig. 12. Partial dynamic recrystallization in this transitional zone led to a more inhomogeneous microstructure. Further plastic deformation in the TMAZ generated some fine grains with high defect density (represented by the black grains in Fig. 12). These high energy grains could become the pitting location during immersion corrosion tests. High strain concentration in the TMAZ resulted in the decrease of corrosion resistance. Moreover, the Cr-rich χ phase was detected in the TMAZ, which also had harmful effects on the corrosion resistance of the TMAZ. Clearly, the FSW joint showed different corrosion behaviors compared to traditional fusion welded joint. The TMAZ, as an inhomogeneous transitional zone in the FSW joint, was confirmed to be the weakest zone to corrosion.

Conclusions

In this work, the microstructure and corrosion resistance of the TMAZ in the FSW joint of HNS were studied in detail. The main conclusions could be summarized as follows:

- The TMAZ, as a transitional region with partial dynamic recrystallization, exhibited a necklace microstructure with an inhomogeneous grain size distribution.
- A high defect density and strain concentration were detected in the fine grain regions of the TMAZ. Fine Cr-rich particles of χ phase were found in this transitional region.
- A high density of pits and deep etched ditches were observed in the TMAZ after immersion corrosion tests, indicating that the TMAZ was the weakest zone to corrosion of the FSW joint.
- A higher corrosion rate in the TMAZ was confirmed by electrochemical tests, significant lower repassivation rate of the TMAZ led to serious corrosion in long term immersion corrosion test. The inferior corrosion resistance of the TMAZ was attributed to high defect density, galvanic corrosion and χ phase precipitation.

Acknowledgments

This work was supported by the National Natural Science Foundation of China [grant Nos. 51671190, 51201163, and 51331008].

References

1. J.W. Simmons,"Overview: High-Nitrogen Alloying of Stainless Steels," *Mater. Sci. Eng. A* 207, 2 (1996): p. 159-169.
2. Y. Fu, X. Wu, E.-H. Han, W. Ke, K. Yang, Z. Jiang,"Effects of Cold Work and Sensitization Treatment on the Corrosion Resistance of High Nitrogen Stainless Steel in Chloride Solutions," *Electrochim. Acta* 54, 5 (2009): p. 1618-1629.
3. U. Kamachi Mudali, P. Shankar, S. Ningshen, R.K. Dayal, H.S. Khatak, B. Raj,"On the Pitting Corrosion Resistance of Nitrogen Alloyed Cold Worked Austenitic Stainless Steels," *Corros. Sci.* 44, 10 (2002): p. 2183-2198.
4. M. Santamaria, F. Di Franco, F. Di Quarto, M. Pisarek, S. Zanna, P. Marcus,"Photoelectrochemical and Xps Characterisation of Oxide Layers on 316l Stainless Steel Grown in High-Temperature Water," *J. Solid State Electrochem.* 19, 12 (2015): p. 3511-3519.
5. T.-H. Lee, S.-J. Kim,"Phase Identification in an Isothermally Aged Austenitic 22cr-21ni-6mo-N Stainless Steel," *Scr. Mater.* 39, 7 (1998): p. 951-956.
6. M. Pohl, O. Storz, T. Glogowski,"Effect of Intermetallic Precipitations on the Properties of Duplex Stainless Steel," *Mater. Charact.* 58, 1 (2007): p. 65-71.
7. E. Erisir, U. Prahl, W. Bleck,"Effect of Precipitation on Hot Formability of High Nitrogen Steels," *Mater. Sci. Eng. A* 528, 1 (2010): p. 519-525.
8. H. Ha, H. Kwon,"Effects of Cr2n on the Pitting Corrosion of High Nitrogen Stainless Steels," *Electrochim. Acta* 52, 5 (2007): p. 2175-2180.
9. I. Woo, Y. Kikuchi,"Weldability of High Nitrogen Stainless Steel," *ISIJ Int.* 42, 12 (2002): p. 1334-1343.
10. R.S. Mishra, Z.Y. Ma,"Friction Stir Welding and Processing," *Mater. Sci. Eng. R* 50, 1-2 (2005): p. 1-78.
11. R.Z. Xu, D.R. Ni, Q. Yang, C.Z. Liu, Z.Y. Ma,"Pinless Friction Stir Spot Welding of Mg–3al–1zn Alloy with Zn Interlayer," *J. Mater. Sci. Technol.* 32, 1 (2016): p. 76-88.
12. D.R. Ni, J.J. Wang, Z.Y. Ma,"Shape Memory Effect, Thermal Expansion and Damping Property of Friction Stir Processed Nitip/Al Composite," *J. Mater. Sci. Technol.* 32, 2 (2016): p. 162-166.
13. T. Okada, S. Machida, T. Nakamura,"Corrosion Resistance Evaluation and Effects of Prior Corrosion and Stress on Fatigue Behavior of Friction Stir Welded Aa2024-T3," *Corrosion* 74, 2 (2018): p. 169-180.
14. L.H. Wu, B.L. Xiao, D.R. Ni, Z.Y. Ma, X.H. Li, M.J. Fu, Y.S. Zeng,"Achieving Superior Superplasticity from Lamellar Microstructure of a Nugget in a Friction-Stir-Welded Ti–6al–4v Joint," *Scr. Mater.* 98, (2015): p. 44-47.
15. D. Wang, D.R. Ni, B.L. Xiao, Z.Y. Ma, W. Wang, K. Yang,"Microstructural Evolution and Mechanical Properties of Friction Stir Welded Joint of Fe–Cr–Mn–Mo–N Austenite Stainless Steel," *Mater. Des.* 64, (2014): p. 355-359.
16. A.P. Reynolds, W. Tang, T. Gnaupel-Herold, H. Prask,"Structure, Properties, and Residual Stress of 304l Stainless Steel Friction Stir Welds," *Scr. Mater.* 48, 9 (2003): p. 1289-1294.
17. S.H.C. Park, Y.S. Sato, H. Kokawa, K. Okamoto, S. Hirano, M. Inagaki,"Corrosion Resistance of Friction Stir Welded 304 Stainless Steel," *Scr. Mater.* 51, 2 (2004): p. 101-105.
18. Y.S. Sato, N. Harayama, H. Kokawa, H. Inoue, Y. Tadokoro, S. Tsuge,"Evaluation of Microstructure and Properties in

Friction Stir Welded Superaustenitic Stainless Steel," *Sci. Technol. Weld. Joining* 14, 3 (2013): p. 202-209.
19. H. Sarlak, M. Atapour, M. Esmailzadeh,"Corrosion Behavior of Friction Stir Welded Lean Duplex Stainless Steel," *Materials & Design (1980-2015)* 66, (2015): p. 209-216.
20. B.W. Ahn, D.H. Choi, D.J. Kim, S.B. Jung,"Microstructures and Properties of Friction Stir Welded 409l Stainless Steel Using a Si3n4 Tool," *Mater. Sci. Eng. A* 532, (2012): p. 476-479.
21. S.H.C. Park, Y.S. Sato, H. Kokawa, K. Okamoto, S. Hirano, M. Inagaki,"Microstructure of Friction-Stir-Welded High-Nitrogen Stainless Steel," *Mater. Sci. Forum* 539-543, (2007): p. 3757-3762.
22. Y. Miyano, H. Fujii, Y. Sun, Y. Katada, S. Kuroda, O. Kamiya,"Mechanical Properties of Friction Stir Butt Welds of High Nitrogen-Containing Austenitic Stainless Steel," *Mater. Sci. Eng. A* 528, 6 (2011): p. 2917-2921.
23. T. Yang, W.-l. Chen, G.-q. Gou, H.-l. Tian, Y. Chen,"Modeling of Corrosion Fatigue Life of Stainless Steel Joints Welded by Laser-Metal Active Gas Hybrid Welding," *Corrosion* 74, 10 (2018): p. 1132-1140.
24. Z. Zhang, H. Jing, L. Xu, Y. Han, L. Zhao, C. Zhou,"Effects of Nitrogen in Shielding Gas on Microstructure Evolution and Localized Corrosion Behavior of Duplex Stainless Steel Welding Joint," *Appl. Surf. Sci.* 404, (2017): p. 110-128.
25. M.A. García-Rentería, V.H. López-Morelos, J. González-Sánchez, R. García-Hernández, L. Dzib-Pérez, F.F. Curiel-López,"Effect of Electromagnetic Interaction During Fusion Welding of Aisi 2205 Duplex Stainless Steel on the Corrosion Resistance," *Appl. Surf. Sci.* 396, (2017): p. 1187-1200.
26. J.M. Aquino, C.A. Della Rovere, S.E. Kuri,"Intergranular and Pitting Corrosion Susceptibilities of a Supermartensitic Stainless Steel Weldment," *Corrosion* 66, 11 (2010): p. 116001-116001-6.
27. M. Ogawa, K. Hiraoka, Y. Katada, M. Sagara, S. Tsukamoto,"Chromium Nitride Precipitation Behavior in Weld Heat-Affected Zone of High Nitrogen Stainless Steel," *ISIJ Int.* 42, 12 (2002): p. 1391-1398.
28. C. Garcia, F. Martin, P. de Tiedra, Y. Blanco, M. Lopez,"Pitting Corrosion of Welded Joints of Austenitic Stainless Steels Studied by Using an Electrochemical Minicell," *Corros. Sci.* 50, 4 (2008): p. 1184-1194.
29. E. Blasco-Tamarit, D.M. García-García, M.I. Ferrándiz, J.G. Antón, A. Guenbour,"Corrosion Resistance and Galvanic Coupling of Uns N08031 Base Metal, Heat-Affected Zone, and Weld Metal in Phosphoric Acid at Different Temperatures," *Corrosion* 67, 3 (2011): p. 035001-035001-035001-035010.
30. A.R. Shankar, S. Niyanth, M. Vasudevan, U.K. Mudali,"Microstructural Characterization and Corrosion Behavior of Activated Flux Gas Tungsten Arc-Welded and Multipass Gas Tungsten Arc-Welded Stainless Steel Weld Joints in Nitric Acid," *Corrosion* 68, 8 (2012): p. 762-773.
31. H.B. Li, Z.H. Jiang, H. Feng, S.C. Zhang, L. Li, P.D. Han, R.D.K. Misra, J.Z. Li,"Microstructure, Mechanical and Corrosion Properties of Friction Stir Welded High Nitrogen Nickel-Free Austenitic Stainless Steel," *Mater. Des.* 84, (2015): p. 291-299.
32. L.N. Brewer, M.A. Othon, L.M. Young, T.M. Angeliu,"Misorientation Mapping for Visualization of Plastic Deformation Via Electron Back-Scattered Diffraction," *Microsc. Microanal.* 12, 1 (2006): p. 85-91.
33. H. Zhang, D. Wang, P. Xue, L.H. Wu, D.R. Ni, Z.Y. Ma,"Microstructural Evolution and Pitting Corrosion Behavior of Friction Stir Welded Joint of High Nitrogen Stainless Steel," *Mater. Des.* 110, (2016): p. 802-810.
34. C.-C. Shih, C.-M. Shih, Y.-Y. Su, S.-J. Lin,"Galvanic Current Induced by Heterogeneous Structures on Stainless Steel Wire," *Corros. Sci.* 47, 9 (2005): p. 2199-2212.
35. M. Shakoori Oskooie, H. Asgharzadeh, S. Sadighikia, M. Salehi,"Significant Corrosion Resistance in an Ultrafine-Grained Al6063 Alloy with a Bimodal Grain-Size Distribution through a Self-Anodic Protection Mechanism," *Metals* 6, 12 (2016):
36. D.E. Williams,"Stochastic Models of Pitting Corrosion of Stainless Steels," *J. Electrochem. Soc.* 132, 8 (1985): p. 1804.
37. G.S. Frankel, L. Stockert, F. Hunkeler, H. Boehni,"Metastable Pitting of Stainless Steel," *Corrosion* 43, 7 (1987): p. 429-436.
38. R.M. Carranza, J.R. Galvele,"Repassivation Kinetics in Stress Corrosion Cracking—I. Type Aisi 304 Stainless Steel in Chloride Solutions," *Corros. Sci.* 28, 3 (1988): p. 233-249.
39. J.R. Galvele, R.M. Torresi, R.M. Carranza,"Passivity Breakdown, Its Relation to Pitting and Stress-Corrosion-Cracking Processes," *Corros. Sci.* 31, (1990): p. 563-571.
40. Z.J. Zheng, Y. Gao, Y. Gui, M. Zhu,"Corrosion Behaviour of Nanocrystalline 304 Stainless Steel Prepared by Equal Channel Angular Pressing," *Corros. Sci.* 54, (2012): p. 60-67.
41. Y.X. Qiao, Y.G. Zheng, W. Ke, P.C. Okafor,"Electrochemical Behaviour of High Nitrogen Stainless Steel in Acidic Solutions," *Corros. Sci.* 51, 5 (2009): p. 979-986.
42. J. Wang, X. Li, J. Wang, E.-h. Han,"Development of a Scratch Electrode System in High Temperature High Pressure Water," *Corros. Sci.* 95, (2015): p. 125-132.
43. J.W. Park, V.S. Rao, H.S. Kwon,"Effects of Nitrogen on the Repassivation Behavior of Type 304l Stainless Steel in Chloride Solution," *Corrosion* 60, 12 (2004): p. 1099-1103.
44. Y. Fu, X. Wu, E. Han, W. Ke, K. Yang, Z. Jiang,"Influence of Cold Work on Pitting Corrosion Behavior of a High Nitrogen Stainless Steel," *J. Electrochem. Soc.* 155, 8 (2008): p. C455.
45. G.A. Zhang, Y.F. Cheng,"Micro-Electrochemical Characterization and Mott–Schottky Analysis of Corrosion of Welded X70 Pipeline Steel in Carbonate/Bicarbonate Solution," *Electrochim. Acta* 55, 1 (2009): p. 316-324.
46. Q.X. Dai, Z.Z. Yuan, X.M. Luo, X.N. Cheng,"Numerical Simulation of Cr2n Age-Precipitation in High Nitrogen Stainless Steels," *Mater. Sci. Eng. A* 385, 1-2 (2004): p. 445-448.
47. Z.B. Wang, N.R. Tao, W.P. Tong, J. Lu, K. Lu,"Diffusion of Chromium in Nanocrystalline Iron Produced by Means of Surface Mechanical Attrition Treatment," *Acta Mater.* 51, 14 (2003): p. 4319-4329.

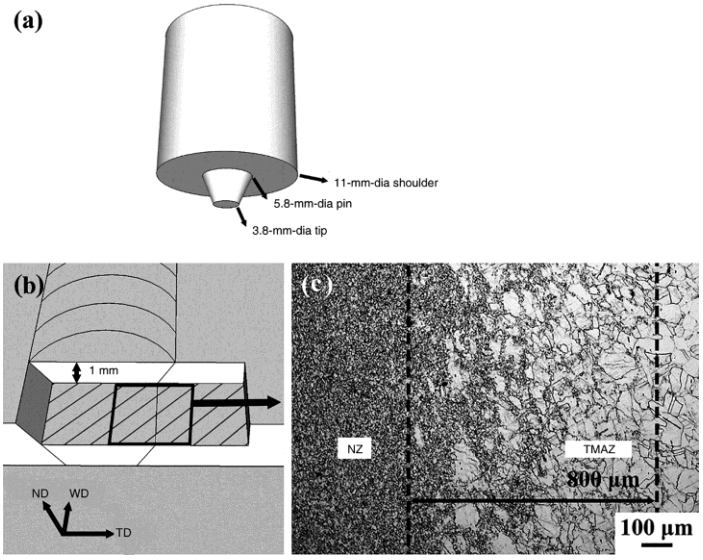

Fig. 1. (a) Schematic diagram of tool for friction stir welding, (b) schematic diagram of specimen preparation for electrochemical tests and (c) microstructure of electrochemical test specimen.

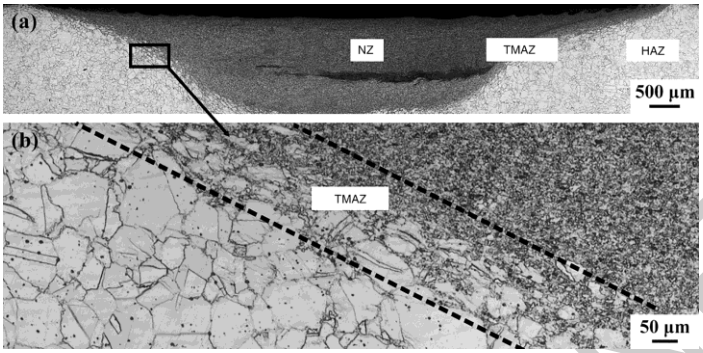

Fig. 2. (a) Cross section of FSW HNS joint and (b) highly deformed microstructure of TMAZ (magnified view of Fig. 1 as pointed out by arrow).

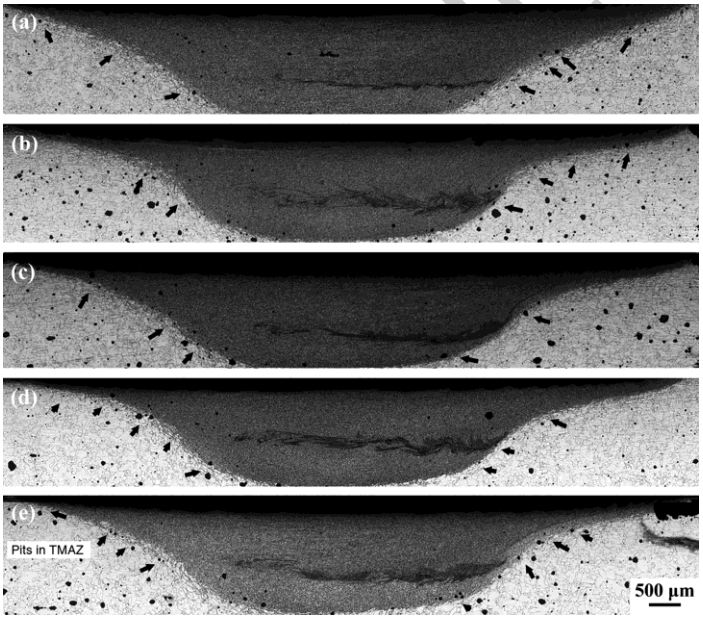

Fig. 3. Cross-sectional macrostructure of FSW HNS joints after ferric chloride pitting test at 50 °C for 48 h and electrolytically etching: (a) 500-50, (b) 500-100, (c) 500-150, (d) 400-100, (e) 600-100.

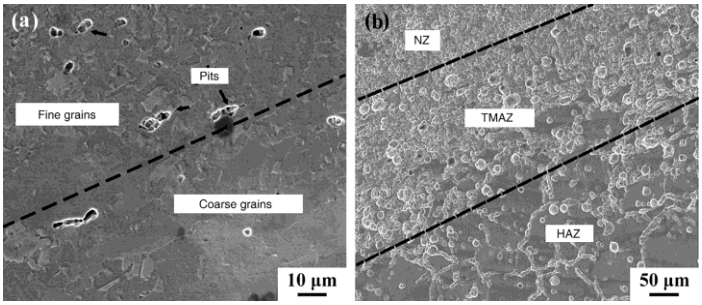

Fig. 4. (a) Magnified view of TMAZ in FSW HNS joint after pitting test for 48 h and (b) magnified TMAZ after ferric sulfate-sulfuric acid intergranular corrosion test for 24 h.

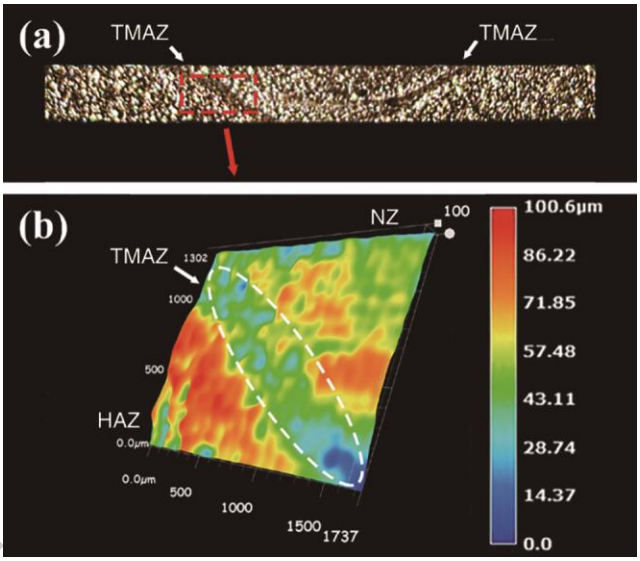

Fig. 5. (a) Corrosion morphology of FSW HNS joint after 60 h intergranular corrosion test and (b) 3D surface corrosion morphology around TMAZ.

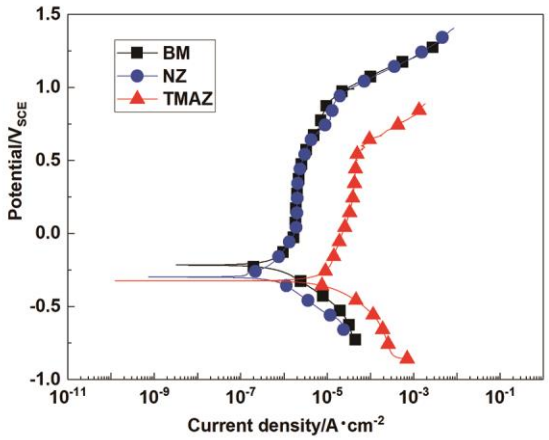

Fig. 6. Potentiodynamic polarization curves of different zones of FSW HNS joint in a 3.5% NaCl solution.

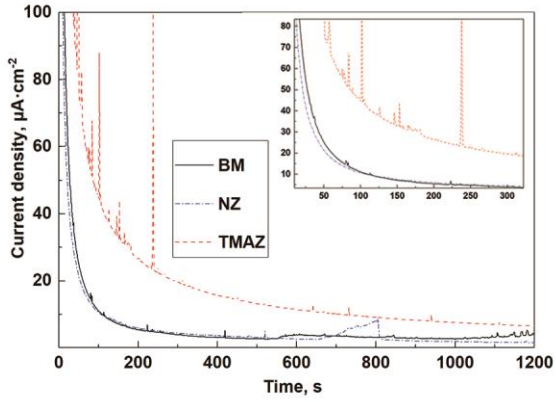

Fig. 7. Current-time transients of different zones of FSW HNS joint.

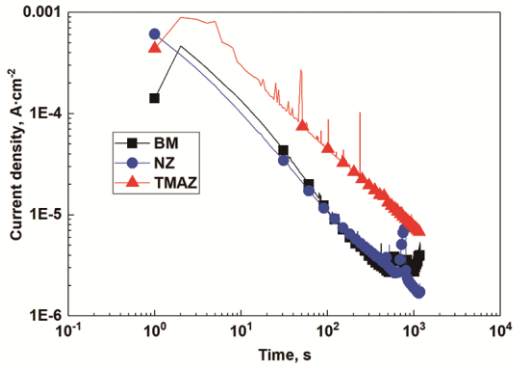

Fig. 8. Double-log plots of current time curves for different zones of FSW HNS joint.

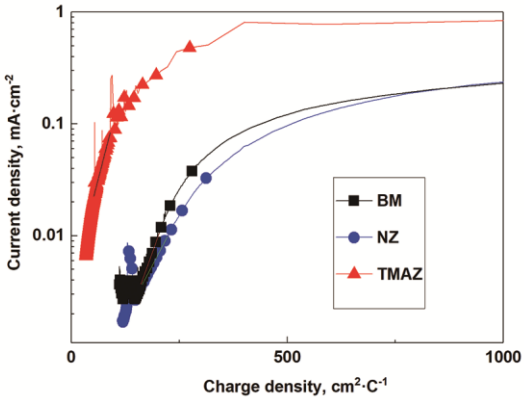

Fig. 9. log$i(t)$ versus $1/Q(t)$ plot of FSW HNS joint.

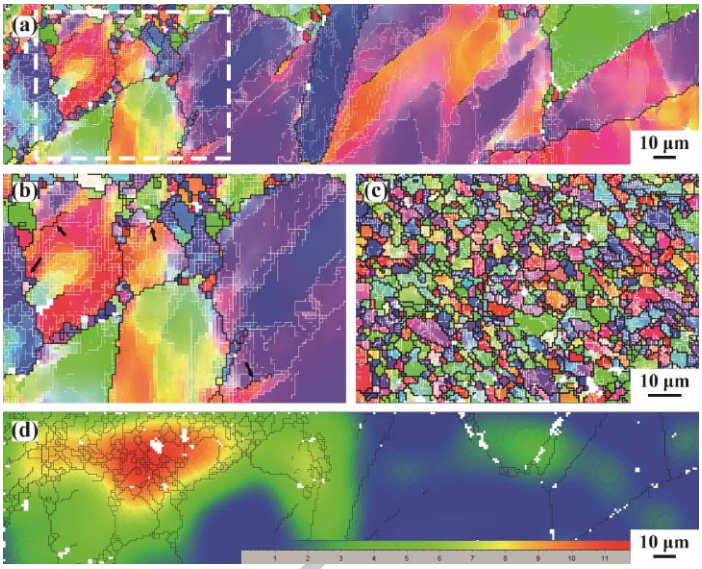

Fig. 10. EBSD maps of (a) TMAZ, (b) a magnified view of selected area in (a), (c) NZ and (d) strain distribution in TMAZ for FSW HNS joint (LAGBs and HAGBs are presented by white and black lines, respectively).

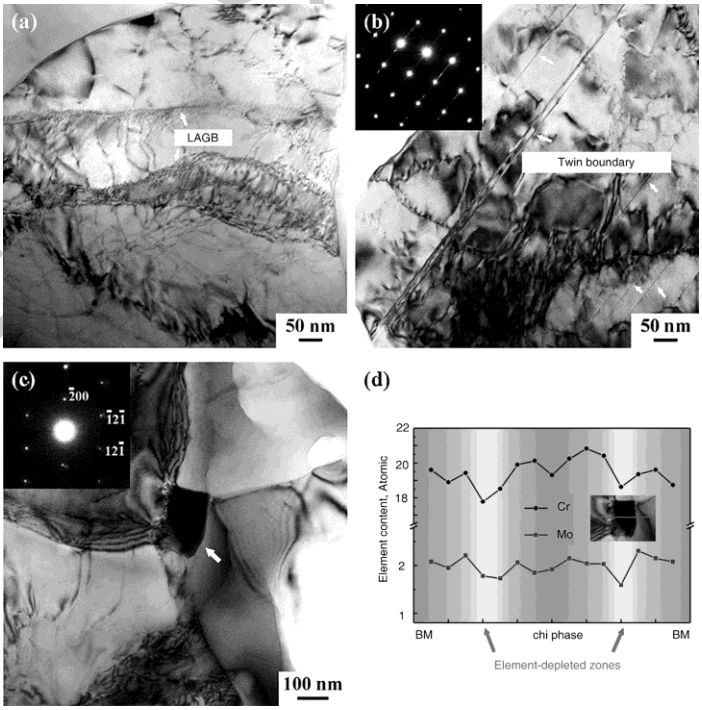

Fig. 11. TEM micrographs of TMAZ in FSW HNS joint showing (a) fine grains with a typical dynamic recovery microstructure, (b) highly deformed microstructure with deformed twins with inserted selected area diffraction (SAD) pattern, (c) chi phase particle with inserted SAD pattern and (d) element content profiles of chi phase.

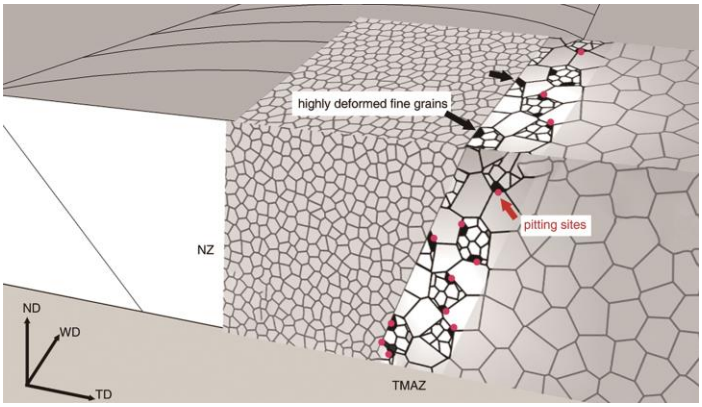

Fig. 12. Illustration of corrosion behavior of TMAZ.

Table 1. Electrochemical parameters of polarization curves for different zones of FSW HNS joint.

	E_{corr} (V_{SCE})	E_{tr} (V_{SCE})	I_p ($A \cdot cm^{-2}$)
BM	-0.28 ± 0.085	1.01 ± 0.120	2.47E-6 ± 4.9E-7
NZ	-0.29 ± 0.014	0.92 ± 0.021	2.55E-6 ± 6.6E-7
TMAZ	-0.25 ± 0.106	0.56 ± 0.049	3.80E-5 ± 7.5E-6